

Cite this: *J. Mater. Chem. A*, 2020, **8**, 6004

Exceptionally high electronic mobility in defect-rich $\text{Eu}_2\text{ZnSb}_{2-x}\text{Bi}_x$ alloys†

Sevan Chanakian,^a David Uhl,^b David Neff,^c Fivos Drymiotis,^c Junsoo Park,^e Valeri Petkov,^d Alexandra Zevalkink^{*a} and Sabah Bux^{*b}

The Zintl compound Eu_2ZnSb_2 was recently shown to have a promising thermoelectric figure of merit, $zT \sim 1$ at 823 K, due to its low lattice thermal conductivity and high electronic mobility. In the current study, we show that further increases to the electronic mobility and simultaneous reductions to the lattice thermal conductivity can be achieved by isovalent alloying with Bi on the Sb site in the $\text{Eu}_2\text{ZnSb}_{2-x}\text{Bi}_x$ series ($x = 0, 0.25, 1, 2$). Upon alloying with Bi, the effective mass decreases and the mobility linearly increases, showing no signs of reduction due to alloy scattering. Analysis of the pair distribution functions obtained from synchrotron X-ray diffraction revealed significant local structural distortions caused by the half-occupied Zn site in this structure type. It is all the more surprising, therefore, to find that Eu_2ZnBi_2 possesses high electronic mobility ($\sim 100 \text{ cm}^2 \text{ V}^{-1} \text{ s}^{-1}$) comparable to that of AM_2X_2 Zintl compounds. The enormous degree of disorder in this series gives rise to exceptionally low lattice thermal conductivity, which is further reduced by Bi substitution due to the decreased speed of sound. Increasing the Bi content was also found to decrease the band gap while increasing the carrier concentration by two orders of magnitude. Applying a single parabolic band model suggests that Bi-rich compositions of $\text{Eu}_2\text{ZnSb}_{2-x}\text{Bi}_x$ have the potential for significantly improved zT ; however, further optimization is necessary through reduction of the carrier concentration to realize high zT .

Received 29th December 2019
Accepted 10th February 2020

DOI: 10.1039/c9ta14170g

rsc.li/materials-a

1. Introduction

Space exploration would not be possible without power for communications and scientific instrumentation. To date, numerous power sources exist including solar and battery technologies; however for deep space exploration past Jupiter, radioisotope thermoelectric generators (RTGs) are the most viable power option.¹ Increasing the efficiency of RTGs through the development of improved thermoelectric materials allows for higher density power systems. Since thermoelectric couples are segmented with materials that are optimized for different temperature ranges,² it is beneficial to develop thermoelectrics that operate efficiently not only at the highest temperatures at the interior of RTGs (1000 °C) but at intermediate temperatures as well (e.g., 400–600 °C). Efficient

thermal-to-electrical energy conversion requires materials with high Seebeck coefficients (α), low electrical resistivity (ρ) and low thermal conductivity (κ), which are embodied in the thermoelectric figure of merit, $zT = \alpha^2 T / \rho \kappa$. This combination of properties is exceptionally difficult to achieve simultaneously posing a fundamental challenge in the development of materials with high zT .^{3–5}

In the past decade, Zintl phases – one of the most structurally diverse classes of intermetallics – have emerged as a promising class of thermoelectric materials at temperatures ranging from room temperature to 1000 °C (e.g., $\text{Yb}_{14}\text{MnSb}_{11}$, Mg_3Sb_2 , and $\text{Ca}_9\text{Zn}_{4.5}\text{Sb}_9$ (ref. 6–22)). Many Zintls exhibit exceptionally low, glass-like lattice thermal conductivity due to either structural complexity⁶ or soft phonon modes.²³ Recently, Chen *et al.* reported promising p-type performance ($zT \sim 1$ at 823 K) in the Zintl compound Eu_2ZnSb_2 .¹¹ The layered structure of Eu_2ZnSb_2 , first reported by D. Wilson *et al.* in 2011,²⁴ is a defect-variant of the AlB_2 structure type containing a 50% vacant Zn site. Chen *et al.* reported a room temperature electronic mobility of $\mu = 65 \text{ cm}^2 \text{ V}^{-1} \text{ s}^{-1}$, which is quite high among Zintl pnictides and surprising given the high concentration of vacancies in the Eu_2ZnSb_2 structure. Additionally, the lattice thermal conductivity, κ_L , was reported to be comparable to that of $\text{Yb}_{14}\text{MnSb}_{11}$, a Zintl phase with a much greater number of atoms per unit cell. The reported $\mu : \kappa_L$ ratio in Eu_2ZnSb_2 is higher than that of any Zintl pnictide currently known.¹¹

^aDepartment of Chemical Engineering and Materials Science, Michigan State University, East Lansing, MI 48824, USA. E-mail: alexzev@msu.edu

^bThermal Energy Conversion Research and Advancement Group, Jet Propulsion Laboratory, Pasadena, CA 91109, USA. E-mail: Sabah.K.Bux@jpl.nasa.gov

^cThermal Energy Conversion Applications & Systems Group, Jet Propulsion Laboratory, Pasadena, CA 91109, USA

^dDepartment of Physics, Central Michigan University, Mt. Pleasant, MI 48859, USA

^eEnergy Technologies Area, Lawrence Berkeley National Laboratory, Berkeley, CA 94720, USA

† Electronic supplementary information (ESI) available. See DOI: 10.1039/c9ta14170g

An improved understanding of disordered materials with high $\mu : \kappa_L$ ratios may open new routes to electron-crystal, phonon-glass behavior in complex semiconductors. In the present study, we investigate the thermoelectric properties of the solid solution between Eu_2ZnSb_2 and Eu_2ZnBi_2 to explore the impact of isovalent alloying on the mobility and thermal conductivity. By substituting Bi on the Sb site, we can probe the effect of increasing the anion, size and thus the degree of orbital overlap, while simultaneously further increasing the degree of site disorder in the system. In addition, pair distribution function analysis was used for the first time in this structure type to study the degree of local structural distortion caused by the half-occupied Zn site.

2. Methods

Synthesis

Polycrystalline $\text{Eu}_2\text{ZnSb}_{2-x}\text{Bi}_x$ samples ($x = 0, 0.25, 1, \text{ and } 2$) were synthesized using a powder metallurgy approach. Stoichiometric amounts of Eu (99.9%, dendritic, Stanford), Zn (99.999%, shot, Alfa Aesar), and Sb (99.99%, shot, Alfa Aesar) and/or Bi (99.999%, shot, Alfa Aesar) were cut or crushed into small pieces for a total of 20 grams. Eu pieces were mechanically cleaned as necessary to remove the oxide layer before weighing. The elements were placed in tungsten carbide vials with two ball bearings and milled for two hours using a SPEX 8000D mixer/mill. To ensure homogenization, the powder was manually scraped and mixed half-way through the milling process. After milling, the powders were placed in 12.7 mm inner-diameter graphite dies and hot pressed for two hours. While Eu_2ZnSb_2 was pressed at 850 °C, the far less refractory Eu_2ZnBi_2 was pressed at 500 °C. The alloy samples were pressed using a linear rule of mixtures (*i.e.* a linear extrapolation from the two pressing temperatures of the parent compositions). The geometric density of all samples were measured to ensure complete sintering and yielded >95% of the theoretical densities.

Structural characterization

The chemical composition of the target phases was determined by electron probe micro-analysis (EPMA) with wavelength dispersive X-ray spectroscopy (WDS) using a JEOL JXA-8200 system. EPMA results are shown in Fig. SI.1.† Powder X-ray diffraction data was collected using a Rigaku Smartlab diffractometer with Cu $K\alpha$ radiation. Lattice parameters were obtained *via* Rietveld refinements completed using Rigaku PDXL software. Additionally, powder $\text{Eu}_2\text{ZnSb}_{2-x}\text{Bi}_x$ samples with $x = 0.25, 1, \text{ and } 2$ were measured at beamline 11-ID-C at the Advanced Photon Source using X-rays with a wavelength of 0.1174 Å. Scattered intensities were recorded with a 2D detector up to a wave vector of $q = 25 \text{ \AA}^{-1}$. The experimental diffraction patterns were converted into atomic pair distribution functions (PDFs). Several structure models were tested and refined against the experimental PDF data using the software PDFgui.²⁵ The initial model used to obtain a structure solution was obtained with the aid of density functional theory (DFT) calculations to

relax the atomic positions in a lower symmetry (space group $C2/c$) superstructure, after which the atomic positions were further refined to fit the experimental PDF.

Computation

Vienna *Ab initio* Simulations Package (VASP)²⁶ was used to perform DFT calculations with projector-augmented wave (PAW)²⁷ pseudopotentials and Perdew–Burke–Ernzerhof (PBE) exchange–correlation functional²⁸ for several different structural models. None of the structure models tested possess a band gap, regardless of the level of theory employed. However, some structure models were found to have energies below the convex hull. The approaches used in this study are described in detail in the ESI.† By using an ordered superstructure (space group $C2/c$) and relaxing the atomic positions, we were able to obtain a structure model that reproduced important features observed in the PDF data.

Electronic and thermal transport characterization

Low temperature Hall coefficients and resistivity were measured using a Quantum Design, Physical Property Measurement System (PPMS) with the Thermal Transport Option (TTO) and AC transport measurement system (ACT) options. For the measurements in this work, a custom AC van der Pauw with field reversal was incorporated.²⁹ Low-temperature Seebeck coefficients were measured using a custom stage in the Quantum Design PPMS. High-temperature Hall coefficients and resistivity were measured using the van der Pauw technique in a four-point probe setup with tungsten electrodes and a reversible 0.8 T magnetic field.³⁰ High-temperature Seebeck coefficients were measured in a custom instrument using W–Nb thermocouples and light-pipe heating as described in ref. 31. The electronic transport data was analyzed using solutions to the Boltzmann transport equation within the relaxation time approximation.³² The room temperature longitudinal and transverse speeds of sound were measured using a Panametrics NDT 5800 pulser/receiver in combination with a Tektronix TDS 1012 digital oscilloscope. Samples were coupled to the pulser/receiver *via* honey. The thermal diffusivity, D , was measured using the laser flash method with a Netzch LFA-457, and thermal conductivity, κ , was subsequently calculated using $\kappa = DC_p d$, where C_p is the Dulong–Petit approximation for heat capacity and d is the geometric density of the sample. An error of approximately ~5% can be assumed for the thermal diffusivity and ~10% for electrical transport measurements.

3. Results and discussion

Characterization of structural disorder

Eu_2ZnSb_2 and Eu_2ZnBi_2 are members of the same A_2ZnPn_2 structure type (space group $P6_3/mmc$), which were first reported by D. Wilson *et al.* in 2011 (ref. 24) and are also formed by a small group of other compounds with $\text{A} = \text{Sr or Eu}$ and $\text{Pn} = \text{P, As, Sb, or Bi}$. The powder XRD patterns of the $\text{Eu}_2\text{ZnSb}_{2-x}\text{Bi}_x$ series, shown in Fig. SI.2,† indicate that the samples are single phase with the exception of small impurity peaks (<5%)

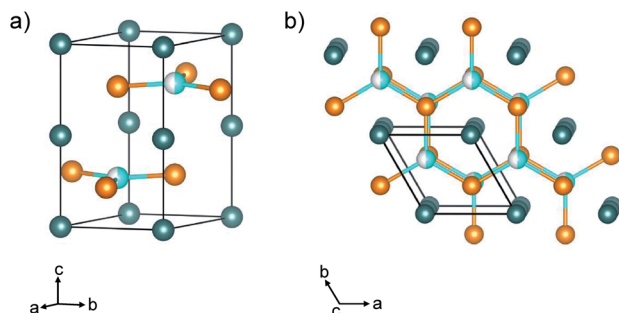


Fig. 1 (a) The nominal structure of Eu_2ZnSb_2 : Eu atoms are shown in teal, Zn atoms in cyan, and Sb in orange. (b) The structure consists of planar hexagonal Zn–Sb nets separated by layers of Eu which occupy the corners and edges of the hexagonal prism. The Zn site is 50% occupied to preserve overall charge neutrality.

identified as EuZn_2Pn_2 . As expected, the lattice parameters of the majority phase increase smoothly with substitution of Bi on the Sb site, confirming the formation of a complete solid solution.

Even in the absence of alloying on the pnictogen site, the half-occupied Zn site in Eu_2ZnSb_2 and Eu_2ZnBi_2 leads to a high degree of local structural disorder that likely affects transport properties. The Eu_2ZnPn_2 structure is a defect variant of the ZrBeSi structure type, which in turn, is a ternary derivative of the AlB_2 structure. In the ZrBeSi structure, Be and Si form planar hexagonal layers in which each Be is coordinated by three Si atoms, and Si is likewise coordinated by three Be atoms. The Zr cations reside between the BeSe layers in hexagonal prisms. Analogously, the Zn and Sb form the planar hexagonal layers in Eu_2ZnSb_2 , and the Eu occupies the hexagonal prisms. However, in contrast to the fully ordered ZrBeSi structure, half of the Zn sites in Eu_2ZnSb_2 are vacant in order to maintain charge neutrality, as shown in Fig. 1a. This leads to an enormous degree of disorder on the anionic sublattice.

Although many possible structures with long-range ordering of Zn vacancies can be envisioned, the observed XRD patterns show no evidence of superstructure peaks. Thus, the nominal structure is the highly symmetric hexagonal unit cell shown in Fig. 1 in which the vacancies are randomly distributed on the Zn site. Despite the lack of long-range order, the Zn vacancies still lead to local distortions of the structure, which we have characterized using pair distribution function (PDF) analysis. As shown in Fig. 2a, the nominal structure fits the PDF pattern for Eu_2ZnBi_2 reasonably well. However, a closer look in Fig. 2b reveals that there are some differences between the experimental and computed data that can only be explained by local deviations from the idealized structure. To obtain a better fit to the experimental PDF, we employed an ordered super-structure with lower symmetry (space group $C2/c$) and relaxed the atomic positions in VASP. This super-structure is able to capture most of the features caused by the local distortions, as shown in Fig. 2c. The deviations from the nominal structure model were found to be due primarily to two factors: variation of the Zn–Bi bond angle (nominally 120 degrees) and corrugation of the nominally planar hexagonal layers. Further details of the

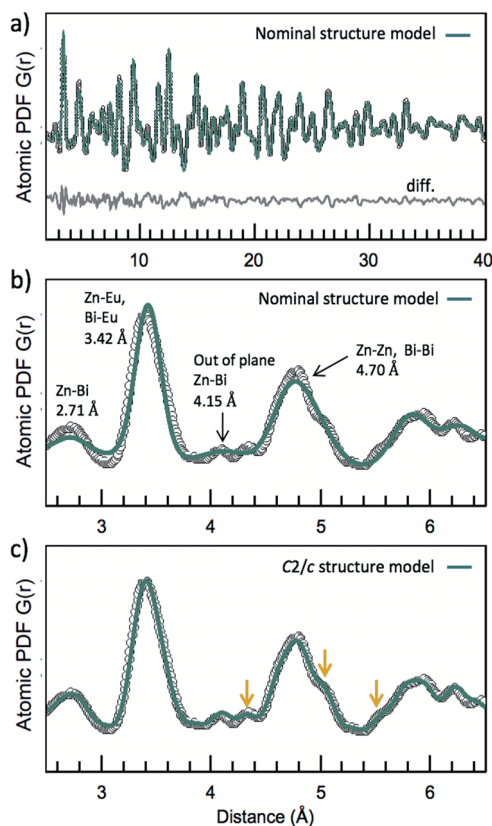


Fig. 2 (a) The experimental PDF of Eu_2ZnBi_2 agrees well with the nominal high-symmetry structure at long length scales. (b) Upon closer inspection, the nominal structure fails to predict nuanced experimental features. (c) A lower symmetry model with distortions in the planar hexagonal Zn–Bi layer captures these finer PDF features, as indicated by the yellow arrows, suggesting that the covalently bonded, planar layers are corrugated.

structural modeling and PDF results for additional $\text{Eu}_2\text{ZnSb}_{2-x}\text{Bi}_x$ samples can be found in the ESI (Fig. SI.3 and SI.4[†]).

Electronic transport

The electronic transport properties of $\text{Eu}_2\text{ZnSb}_{2-x}\text{Bi}_x$ ($x = 0, 0.5, 1, 2$) samples measured from 10–800 K are shown in Fig. 3. The temperature-dependent resistivity (ρ) shown in Fig. 3a confirms that un-alloyed Eu_2ZnSb_2 is a highly resistive non-degenerate semiconductor, consistent with previous reports by Chen *et al.* This is also consistent with electron counting, which, in the limit of complete electron transfer, can be written as $[\text{Eu}^{2+}]_2[\text{Zn}_{1/2}^{2+}\text{Sb}^{3-}]_2^{2-}$ to yield a valence precise stoichiometry. As the Bi concentration is increased, the resistivity decreases by more than two orders of magnitude with a corresponding shift from a non-degenerate to degenerate semiconducting temperature-dependence.

The drastic change in resistivity is due to simultaneous increases in the carrier concentration and carrier mobility, as shown in Fig. 3b and c. Although Bi and Sb are isovalent, there is a 100-fold increase in carrier concentration upon fully substituting Sb with Bi. This indicates that a significant increase in defect concentration occurs with increasing Bi

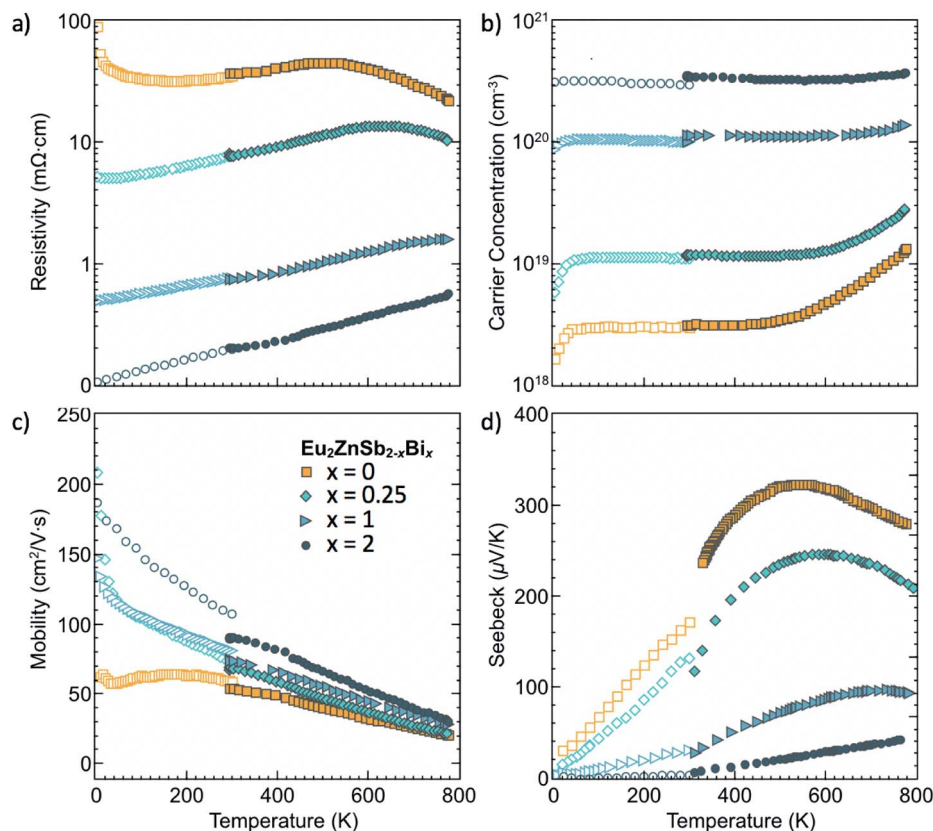


Fig. 3 Increasing the Bi content, x , leads to (a) decreased resistivity due to (b) an increase in the Hall carrier concentration and (c) mobility. (d) The Seebeck coefficients decrease with the increase in carrier concentration accordingly.

concentration and/or a decrease in the band gap. From previous studies of defect formation in chemically similar Zintl pnictides, vacancies on the Eu site (V_{Eu}^{2-}) are the defects most likely to contribute to the structure's p-type behavior.^{10,33,34} Acceptor-type vacancies on the Zn site (V_{Zn}^{2-}) are another possible explanation, consistent with the study by Chen *et al.* in which increased carrier concentration was achieved by synthesizing samples with compositions $\text{Eu}_2\text{Zn}_{1-x}\text{Sb}_2$. We note, however, that the Zn site is already 50% vacant in this structure type, meaning a stoichiometry of $\text{Eu}_2\text{Zn}_{1-x}\text{Pn}_2$ corresponds to a Zn occupancy of $(1-x)/2$. Unfortunately, the disordered nature of the Zn-site and lack of long-range order in this system makes computational determination of defects energies prohibitive.

The Seebeck coefficients of the $\text{Eu}_2\text{ZnSb}_{2-x}\text{Bi}_x$ series are shown in Fig. 3d. Eu_2ZnSb_2 exhibits the highest Seebeck

coefficients, which begin to peak at approximately 550 K before beginning to decrease. This decrease is due to minority carrier activation, as evidenced by the exponentially increasing Hall carrier concentration at coinciding temperatures. With increasing Bi content and carrier concentration, the onset of minority carrier activation is shifted towards higher temperatures. We can approximate the band gaps (E_g) using the Goldsmid–Sharp approximation, $E_g = 2T_{\text{max}}\alpha_{\text{max}}$, which yields $E_g = 0.34$ eV, 0.29 eV, and 0.14 eV for the samples with $x = 0$, 0.25, and 1, respectively (Table 1). For $x = 2$, the Seebeck coefficient increases linearly within the entire measured temperature range, so a band gap could not be estimated. However, the observed trend in E_g vs. x suggests that the gap for $x = 0$ is quite small, possibly zero.

Table 1 Electronic and thermal properties of the $\text{Eu}_2\text{ZnSb}_{2-x}\text{Bi}_x$ series. E_g was estimated using the Goldsmid–Sharp approximation, the effective mass (m_{SPB}^*) and intrinsic mobility (μ_0) were estimated using a single parabolic band model, and the elastic moduli (G , K) and speed of sound (v_L and v_T) were obtained from ultrasound measurements

	E_g (eV)	m_{SPB}^* @ 573 K (m_e)	μ_0 @ 573 K ($\text{cm}^2 \text{V}^{-1} \text{s}^{-1}$)	G (GPa)	K (GPa)	v_L (m s^{-1})	v_T (m s^{-1})	κ_L (W mK^{-1})
Eu_2ZnSb_2 ($x = 0$)	0.34	0.57	44	28	42	2030	3440	0.43
$\text{Eu}_2\text{ZnSb}_{1.75}\text{Bi}_{0.25}$ ($x = 0.25$)	0.29	0.61	48	—	—	—	—	—
Eu_2ZnSbBi ($x = 1$)	0.14	0.51	88	—	—	—	—	—
Eu_2ZnBi_2 ($x = 2$)	>0.06	0.32	181	21	35	1580	2750	0.33

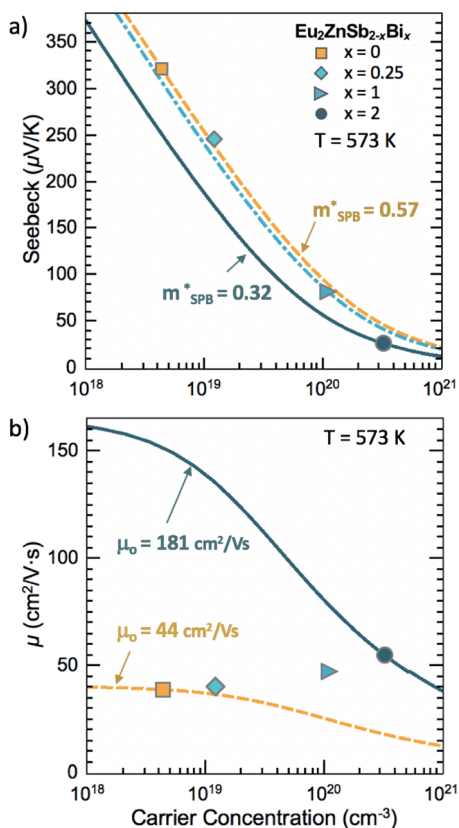


Fig. 4 (a) The Seebeck coefficients and (b) mobility at 573 K show, respectively, a decrease in m_{SPB}^* , and a large increase in the intrinsic mobility, μ_0 , as the Bi concentration increases. The curves were generated using an SPB model under the assumption of acoustic phonon scattering.

Fig. 4a shows the relationship between the Seebeck coefficients and carrier concentration, n , measured at 573 K. As expected, increasing n leads to a decrease in the Seebeck coefficient. The three curves in Fig. 4a were generated using a single parabolic band (SPB) model under an assumption of acoustic phonon scattering. Eu_2ZnSb_2 exhibits an SPB effective mass of approximately $m_{\text{SPB}}^* = 0.57m_e$, consistent with prior results from Chen *et al.*,¹¹ while the effective mass of Eu_2ZnBi_2 is reduced to $0.32m_e$. In contrast, the varying Zn content used by Chen *et al.* to increase the carrier concentration of Eu_2ZnSb_2 had no impact on m^* . Note that there is considerable uncertainty in the estimated m^* , arising from the sum of the uncertainty in the Seebeck coefficients and carrier concentrations.

The mobility, μ , of Eu_2ZnSb_2 , calculated from $\rho = 1/ne\mu$, is approximately $50 \text{ cm}^2 \text{ V}^{-1} \text{ s}^{-1}$ at room temperature, consistent with reports by Chen *et al.*¹¹ At low temperatures (10–200 K), the positive slope of μ in Eu_2ZnSb_2 is indicative of a resistive grain boundary contribution¹⁶ or scattering from ionized impurities. With increasing Bi content, the slope of the low-temperature mobility shifts from positive to negative, indicating a transition towards acoustic phonon-dominated scattering. In pure Eu_2ZnBi_2 , the mobility is consistent with acoustic phonon scattering ($\mu \propto T^{-1.5}$) across the entire measured temperature range and reaches a maximum of $180 \text{ cm}^2 \text{ V}^{-1} \text{ s}^{-1}$ at 10 K. The

high mobility in both Eu_2ZnSb_2 and Eu_2ZnBi_2 is comparable to the rare-earth containing AM_2Pn_2 compounds,^{12,35,36} which is exceptional given the enormous degree of disorder and local distortions on the anion sublattice in this structure.^{33,37–39}

As shown in Fig. 4b, μ does not decrease with increasing carrier concentration as expected within a single parabolic band model with acoustic phonon scattering. Rather, μ increases strongly as a function of Bi-content and carrier concentration. The introduction of point defects *via* alloying on the pnictogen site would also be expected to substantially reduce μ due to the mass contrast between Sb and Bi, but no such effect is observed here. One possible explanation is that the scattering due to the partially occupied Zn site (and associated local structural distortions) is the dominant factor, essentially obscuring the impact of further point defect scattering.

The complete substitution of Bi on the pnictogen site leads to a four-fold increase in the intrinsic mobility, μ_0 (see the solid and dashed curves in Fig. 4b). The difference between μ_0 of the two end-members can be attributed to the significant decrease in the effective mass with Bi alloying. As discussed in ref. 40, the relationship between mobility and effective mass in the limit of deformation-potential scattering (*e.g.*, acoustic-phonon scattering) is given by $\mu \propto 1/(m^*)^{5/2}$. Thus, assuming the change in m^* results from a change in band curvature (as opposed to a change in degeneracy), a roughly two-fold reduction in m^* can lead to a four-fold increase in mobility, consistent with the observed increase in intrinsic mobility shown in Fig. 4b.

The trend towards smaller band gaps and higher mobility in compounds with larger anions has been observed in a number of other Zintl compounds, including the AM_2Pn_2 compounds (A = alkaline or rare earth, M = metal, Pn = pnictogen)³³ and the $\text{Mg}_3\text{Sb}_{2-x}\text{Bi}_x$ system.⁴¹ The basic trend can be understood by considering the relative ionization energy, electronegativity, and atomic size of the anions. As the ionization energy and electronegativity of the anion increases, the energy of the bonding molecular orbital decreases.⁴² This results in a larger energy difference between the bonding and antibonding states in the solid which would yield a larger gap. However, as the atomic size increases, orbital overlap of the anion states increases, which broadens the bands and simultaneously leads to greater dispersion (smaller effective mass) and a small band gap.

Thermal transport

Fig. 5a shows the total thermal conductivity, κ_{total} , of the $\text{Eu}_{2-x}\text{ZnSb}_{2-x}\text{Bi}_x$ samples. Increased electronic conductivity in the Bi-containing samples results in a considerable increase in the total thermal conductivity. In order to approximate the electronic contribution, κ_e , the Wiedemann–Franz approximation ($\kappa_e = LT/\rho$) was used for samples with $x = 0, 0.25$, and 1 with Lorenz number, L , determined by the SPB model.⁴³ Subtracting κ_e from κ_{total} yields the lattice contribution, κ_L , shown in Fig. 5b. The exceptionally low, nearly temperature-independent lattice thermal conductivity of these samples can be attributed to the local distortions from the half-occupied Zn site as well as the mixed pnictogen site occupation. When applied to the Eu_2ZnBi_2

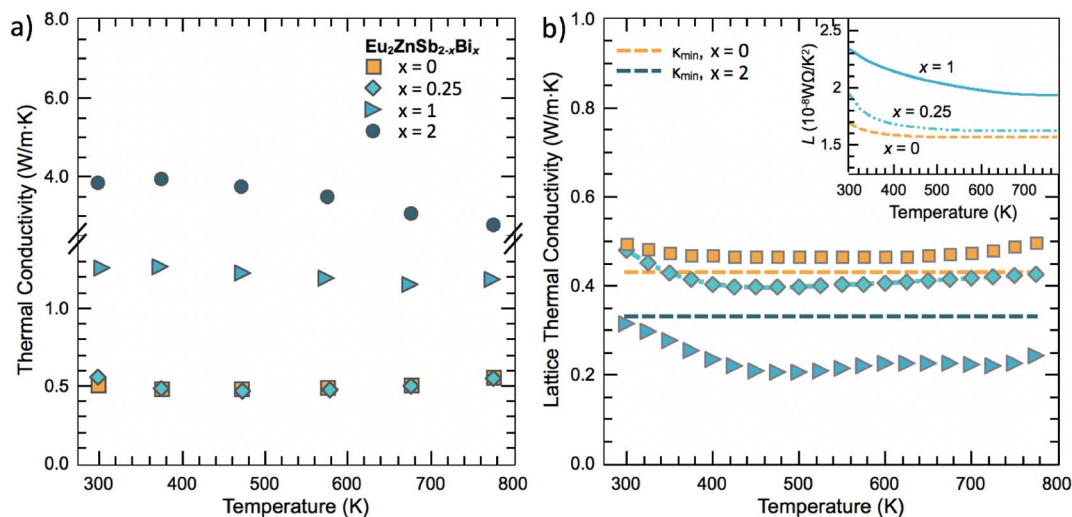


Fig. 5 The (a) total and (b) lattice thermal conductivity of the $\text{Eu}_2\text{ZnSb}_{2-x}\text{Bi}_x$ series. Across the entire temperatures range, κ_L is at or below the glassy limit (orange dashed line for Eu_2ZnSb_2 and blue dashed line for Eu_2ZnBi_2). The inset illustrates the temperature dependence of the SPB Lorenz numbers: note the $x = 2$ composition is not included in the plot as it predicts unrealistic negative lattice thermal conductivity values.

sample ($x = 2$), the Wiedemann–Franz approximation yields an unrealistically high electronic contribution, which, in turn, leads to a negative lattice thermal conductivity for all temperatures above 400 K. This is shown in Fig. SI.4,[†] which compares the κ_L values for Eu_2ZnBi_2 that were obtained using different assumptions, including the insulating and metallic limits of the Lorenz number. Failure of the Wiedemann–Franz approximation is not uncommon in systems that combine very low lattice thermal conductivity with high electronic conductivity.⁴⁴ Overestimations of the Lorenz number (L) can also stem from deviations from a single parabolic band system.⁴⁵ Because we cannot confidently assign a κ_L value to the Eu_2ZnBi_2 sample, we instead show the Cahill glassy minimum, κ_{min} , estimated using the experimental speed of sound (see Table 1). The predicted glassy minimum for Eu_2ZnBi_2 is slightly lower than that of Eu_2ZnSb_2 due to the shorter, stiffer bonds of the Sb analogue, which lead to its larger G and K reported in Table 1.

Figure of merit

The figure of merit, zT , of the $\text{Eu}_2\text{ZnSb}_{2-x}\text{Bi}_x$ samples is shown in Fig. 6a. Eu_2ZnSb_2 has a maximum zT of 0.5 while the sample with $x = 0.25$ reaches a slightly improved maximum of 0.6 at 800 K. This is slightly lower than the zT reported by Chen *et al.* ($zT = 0.6$ at 720 K and 0.575 at 800 K) for un-altered Eu_2ZnSb_2 .¹¹ As previously discussed, the m_{SPB}^* and κ_L of the samples vary as a function of Bi concentration, so each sample was fit to an individual SPB model using the parameters summarized in Table 1. According to the model (dashed curves in Fig. 6b), the optimum carrier concentration required to maximize zT decreases as Bi concentration increases. This is attributed to the combined impact of increased mobility (see Fig. 4) and lower lattice thermal conductivity. Thus, while Eu_2ZnSb_2 has been reported to have a zT of 1 at 823 K, significantly higher zT values are anticipated for samples alloyed with Bi (assuming the carrier concentration can be optimized).

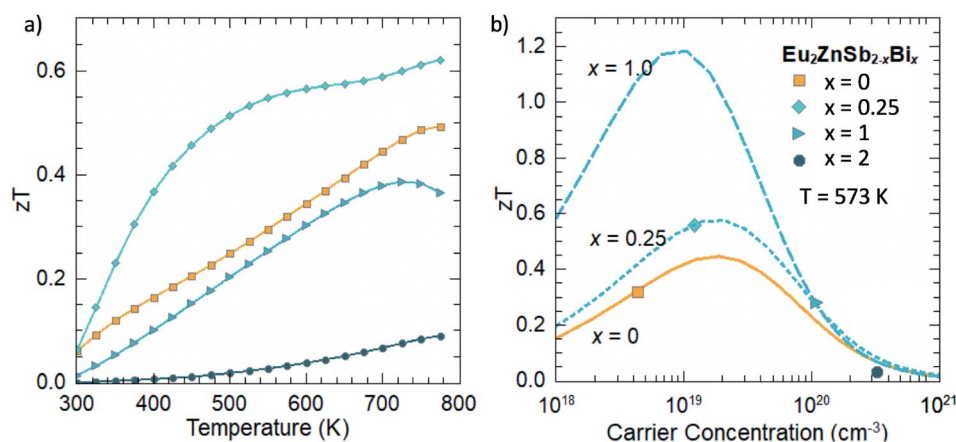


Fig. 6 (a) The figure of merit, zT , reaches a maximum of 0.6 at 573 K for the $x = 0.25$ composition. (b) SPB models (dashed curves) show that as x increases, the carrier concentration required to optimize zT will decrease. The symbols show the experimental zT values at 573 K. The highest zT values are anticipated in the $x = 1$ sample if n can be optimized.

Although the SPB curve is not shown for the end-member compound Eu_2ZnBi_2 , it has an even lighter effect mass than Eu_2ZnBiSb ($x = 1$), which shifts the predicted optimal carrier concentration to well below 10^{19} . Further, assuming that $\kappa_L = \kappa_{\text{min}}$ for Eu_2ZnBi_2 , which is a conservative estimate in this case, one would predict a peak zT of ~ 1.5 at 573 K. However, this prediction is misleading and is a direct consequence of our “single band” assumption, which does not account for minority carriers. In reality, effects such as minority carrier activation and bipolar thermal conductivity would likely reduce the maximum zT value. The band gap of Eu_2ZnBi_2 is estimated to be roughly 0.06 to 0.14 eV using the Goldsmid–Sharp approximation. However, it is possible that Eu_2ZnBi_2 does not have a bandgap. Another challenge lies in fighting compensating defects in order to dope Eu_2ZnBi_2 to carrier concentrations below 10^{19} cm^{-3} . However, these obstacles might be less prominent in the alloyed compositions, providing us with a path to synthesizing high zT materials in the low-to mid-temperature regime.

4. Conclusion

The $\text{Eu}_2\text{ZnSb}_{1-x}\text{Bi}_x$ system is exceptional in that it exhibits very high electronic mobility despite an immense degree of local structural disorder. This was hinted at in a previous investigation by Chen *et al.*, which showed that among all Zintl compounds, Eu_2ZnSb_2 appears to have the highest ratio of mobility to lattice thermal conductivity. In the current study, we have revealed the full extent of the local disorder caused by Zn vacancies in this material using pair distribution function analysis. Furthermore, we have shown that additional disorder in the form of Bi substitution on the Sb site has no adverse impact on the mobility. In fact, the mobility increases linearly with Bi alloying, leading to an overall increase of a factor of two in the Bi end-member. Simultaneously, the lattice thermal conductivity decreases with increasing Bi substitution. Thus, even using conservative approximations, Eu_2ZnBi_2 now has the highest $\mu : \kappa_L$ ratio of any Zintl compound reported to date. The remarkably high electronic mobility in this highly disordered material system points to a new path forward in the never-ending quest for new materials with phonon-glass electron-crystal behavior.

Conflicts of interest

There are no conflicts to declare.

Acknowledgements

The majority of this work was performed at the California Institute of Technology/Jet Propulsion Laboratory under contract with the National Aeronautics and Space Administration. This work was supported by the NASA Science Missions Directorate under the Radioisotope Power Systems Program's Thermoelectric Technology Development Project. S. C. and A. Z. were supported by the National Science Foundation (NSF) award number 1709158. S. C.'s contributions are based upon

work supported by the National Science Foundation Graduate Research Fellowship Program award number DGE-1848739. Any opinions, findings, and conclusions or recommendations expressed in this material are those of the author(s) and do not necessarily reflect the views of the National Science Foundation. Structural analysis performed by V. P. was supported by DOE-BES grant DE-SC0006877 and used resources of the Advanced Photon Source at the Argonne National Laboratory provided by the DOE Office of Science under contract no. DE-AC02-06CH11357. Computation by J. P. was supported by funding from the U.S. Department of Energy, Office of Basic Energy Sciences, Early Career Research Program. This work used computational time and resources of the National Energy Research Scientific Computing Center, a DOE Office of Science User Facility supported by the Office of Science of the U.S. Department of Energy under Contract No. DE-AC02-05CH11231. S. C. would like to acknowledge Max Wood for his discussions and paper referrals and Kristen McLean for her experimental contributions.

Notes and references

- 1 D. M. Rowe, Applications of Nuclear-Powered Thermoelectric Generators in Space, *Appl. Energy*, 1991, **40**(4), 241–271, DOI: 10.1016/0306-2619(91)90020-X.
- 2 T. Caillat, J. P. Fleurial, G. N. Snyder, A. Zoltan, D. Zoltan and A. Borshchevsky, Development of a High Efficiency Thermoelectric Unicouple for Power Generation Applications, *Eighteenth Int. Conf. Thermoelectr. Proceedings, ICT'99*, 1999.
- 3 F. J. DiSalvo, Thermoelectric Cooling and Power Generation, *Science*, 1999, **285**(5428), 703–706.
- 4 A. Zevalkink, D. M. Sniadak, J. L. Blackburn, A. J. Ferguson, M. L. Chabynec, O. Delaire, J. Wang, K. Kovnir, J. Martin, L. T. Schelhas, *et al.*, A Practical Field Guide to Thermoelectrics: Fundamentals, Synthesis, and Characterization, *Appl. Phys. Rev.*, 2018, **5**(2), 021303, DOI: 10.1063/1.5021094.
- 5 G. J. Snyder and E. S. Toberer, Complex Thermoelectric Materials, *Nat. Mater.*, 2008, **7**, 105–114.
- 6 E. S. Toberer, A. Zevalkink and G. J. Snyder, Phonon Engineering through Crystal Chemistry, *J. Mater. Chem.*, 2011, **21**(40), 15843.
- 7 E. S. Toberer, C. A. Catherine, S. R. Brown, T. Ikeda, A. F. May, S. M. Kauzlarich and G. J. Snyder, Traversing the Metal-Insulator Transition in a Zintl Phase: Rational Enhancement of Thermoelectric Efficiency in $\text{Yb}_{14}\text{Mn}_{1-x}\text{Al}_x\text{Sb}_{11}$, *Adv. Funct. Mater.*, 2008, **18**(18), 2795–2800.
- 8 S. Bobev, J. D. Thompson, J. L. Sarrao, M. M. Olmstead, H. Hope and S. M. Kauzlarich, Probing the Limits of the Zintl Concept: Structure and Bonding in Rare-Earth and Alkaline-Earth Zinc-Antimonides $\text{Yb}_9\text{Zn}_{4+x}\text{Sb}_9$ and $\text{Ca}_9\text{Zn}_{4.5}\text{Sb}_9$, *Inorg. Chem.*, 2004, **43**(16), 5044–5052.
- 9 S. Ohno, U. Aydemir, M. Amsler, J.-H. Pöhls, S. Chanakian, A. Zevalkink, M. A. White, S. K. Bux, C. Wolverton and G. J. Snyder, Achieving $ZT > 1$ in Inexpensive Zintl Phase

- $\text{Ca}_9\text{Zn}_{4+x}\text{Sb}_9$ by Phase Boundary Mapping, *Adv. Funct. Mater.*, 2017, **27**(20), 1606361.
- 10 H. Tamaki, H. K. Sato and T. Kanno, Isotropic Conduction Network and Defect Chemistry in $\text{Mg}_{(3+\delta)}\text{Sb}_2$ -Based Layered Zintl Compounds with High Thermoelectric Performance, *Adv. Mater.*, 2016, **28**(46), 10182–10187.
 - 11 Y. Chen, W. Xue, S. Li, Z. Zhang, X. Li, X. Wang, Y. Liu, J. Sui, X. Liu, F. Cao, *et al.*, Zintl-Phase Eu_2ZnSb_2 : A Promising Thermoelectric Material with Ultralow Thermal Conductivity, *Proc. Natl. Acad. Sci. U. S. A.*, 2019, **116**(8), 2831–2836, DOI: 10.1073/pnas.1819157116.
 - 12 J. Shuai, J. Mao, S. Song, Q. Zhang, G. Chen and Z. Ren, Recent Progress and Future Challenges on Thermoelectric Zintl Materials, *Materials Today Physics*, 2017, **1**, 74–95.
 - 13 S. M. Kauzlarich, S. R. Brown and G. J. Snyder, Zintl Phases for Thermoelectric Devices, *Dalton Trans.*, 2007, 2099–2107.
 - 14 J. Zhang, L. Song, S. H. Pedersen, H. Yin, L. T. Hung and B. B. Iversen, Discovery of High-Performance Low-Cost n-Type Mg_3Sb_2 -Based Thermoelectric Materials with Multi-Valley Conduction Bands, *Nat. Commun.*, 2017, **8**, 13901.
 - 15 H. Tamaki, H. K. Sato and T. Kanno, Isotropic Conduction Network and Defect Chemistry in $\text{Mg}_{3+\delta}\text{Sb}_2$ -Based Layered Zintl Compounds with High Thermoelectric Performance, *Adv. Mater.*, 2016, **28**(46), 10182–10187.
 - 16 J. J. Kuo, S. D. Kang, K. Imasato, H. Tamaki, S. Ohno, T. Kanno and G. J. Snyder, Grain Boundary Dominated Charge Transport in Mg_3Sb_2 -Based Compounds, *Energy Environ. Sci.*, 2018, **11**, 429.
 - 17 U. Aydemir, A. Zevalkink, A. Ormeci, S. Bux and G. J. Snyder, Enhanced Thermoelectric Properties of the Zintl Phase BaGa_2Sb_2 via Doping with Na or K, *J. Mater. Chem.*, 2016, **4**, 1867–1875.
 - 18 U. Aydemir, A. Zevalkink, A. Ormeci, Z. M. Gibbs, S. Bux and G. J. Snyder, Thermoelectric Enhancement in BaGa_2Sb_2 by Zn Doping, *Chem. Mater.*, 2015, **27**, 1622–1630.
 - 19 X. Shi, C. Sun, Z. Bu, X. Zhang, Y. Wu, S. Lin, W. Li, A. Faghaninia, A. Jain and Y. Pei, Revelation of Inherently High Mobility Enables Mg_3Sb_2 as a Sustainable Alternative to N- Bi_2Te_3 Thermoelectrics, *Adv. Sci.*, 2019, **6**(16), 1802286, DOI: 10.1002/advs.201802286.
 - 20 T. Kanno, H. Tamaki, H. K. Sato, S. D. Kang, S. Ohno, K. Imasato, J. J. Kuo, G. J. Snyder and Y. Miyazaki, Enhancement of Average Thermoelectric Figure of Merit by Increasing the Grain-Size of $\text{Mg}_{3.2}\text{Sb}_{1.5}\text{Bi}_{0.49}\text{Te}_{0.01}$, *Appl. Phys. Lett.*, 2018, **112**(3), 33903, DOI: 10.1063/1.5016488.
 - 21 K. Imasato, S. D. Kang and G. J. Snyder, Exceptional Thermoelectric Performance in $\text{Mg}_3\text{Sb}_{0.6}\text{Bi}_{1.4}$ for Low-Grade Waste Heat Recovery, *Energy Environ. Sci.*, 2019, **12**(3), 965–971, DOI: 10.1039/c8ee03374a.
 - 22 X. Shi, T. Zhao, X. Zhang, C. Sun, Z. Chen, S. Lin, W. Li, H. Gu and Y. Pei, Extraordinary N-Type Mg_3SbBi Thermoelectrics Enabled by Yttrium Doping, *Adv. Mater.*, 2019, **31**(36), 1903387, DOI: 10.1002/adma.201903387.
 - 23 W. Peng, G. Petretto, G.-M. Rignanese, G. Hautier and A. Zevalkink, An Unlikely Route to Low Lattice Thermal Conductivity: Small Atoms in a Simple Layered Structure, *Joule*, 2018, **2**(9), 1879–1893.
 - 24 D. K. Wilson, B. Saporov and S. Bobev, Synthesis, Crystal Structures and Properties of the Zintl Phases Sr_2ZnP_2 , Sr_2ZnAs_2 , A_2ZnSb_2 and A_2ZnBi_2 (A = Sr and Eu), *Z. Anorg. Allg. Chem.*, 2011, **637**(13), 2018–2025.
 - 25 C. L. Farrow, P. Juhas, J. W. Liu, D. Bryndin, E. S. Božin, J. Bloch, Th. Proffen and S. J. L. Billinge, PDFfit2 and PDFgui: Computer Programs for Studying Nanostructure in Crystals, *J. Phys.: Condens. Matter*, 2007, **19**(33), 335219.
 - 26 G. Kresse and J. Furthmüller, Efficiency of Ab-Initio Total Energy Calculations for Metals and Semiconductors Using a Plane-Wave Basis Set, *Comput. Mater. Sci.*, 1996, **6**, 15–50.
 - 27 J. P. Perdew, K. Burke and M. Ernzerhof, Generalized Gradient Approximation Made Simple, *Phys. Rev. Lett.*, 1996, **77**, 3865–3868.
 - 28 P. E. Blöchl, Projector Augmented-Wave Method, *Phys. Rev. B: Condens. Matter Mater. Phys.*, 1994, **50**(24), 17953.
 - 29 K. A. Borup, J. De Boor, H. Wang, F. Drymiotis, F. Gascoin, X. Shi, L. Chen, M. I. Fedorov, E. Müller, B. B. Iversen, *et al.*, Measuring Thermoelectric Transport Properties of Materials, *Energy Environ. Sci.*, 2015, **8**, 423–435.
 - 30 K. A. Borup, E. S. Toberer, L. D. Zoltan, G. Nakatsukasa, M. Errico, J. P. Fleurial, B. B. Iversen and G. J. Snyder, Measurement of the Electrical Resistivity and Hall Coefficient at High Temperatures, *Rev. Sci. Instrum.*, 2012, **83**(12), 123902.
 - 31 C. Wood, D. Zoltan and G. Stapfer, Measurement of Seebeck Coefficient Using a Light Pulse, *Rev. Sci. Instrum.*, 1985, **56**, 719.
 - 32 A. F. May, E. S. Toberer, A. Saramat and G. J. Snyder, Characterization and Analysis of Thermoelectric Transport in N-Type $\text{Ba}_8\text{Ga}_{16-x}\text{Ge}_{30+x}$, *Phys. Rev. B: Condens. Matter Mater. Phys.*, 2009, **80**(12), 125205.
 - 33 W. Peng, S. Chanakian and A. Zevalkink, Crystal Chemistry and Thermoelectric Transport of Layered AM_2X_2 Compounds, *Inorg. Chem. Front.*, 2018, **5**, 1744–1759.
 - 34 G. S. Pomrehn, A. Zevalkink, W. G. Zeier, A. van de Walle and G. J. Snyder, Defect-Controlled Electronic Properties in AZn_2Sb_2 Zintl Phases, *Angew. Chem., Int. Ed. Engl.*, 2014, **53**(13), 3422–3426.
 - 35 H. Zhang, J. T. Zhao, Y. Grin, X. J. Wang, M. B. Tang, Z. Y. Man, H. H. Chen and X. X. Yang, A New Type of Thermoelectric Material, EuZn_2Sb_2 , *J. Chem. Phys.*, 2008, **129**(16), 164713.
 - 36 J. Shuai, H. Geng, Y. Lan, Z. Zhu, C. Wang, Z. Liu, J. Bao, C.-W. Chu, J. Sui and Z. Ren, Higher Thermoelectric Performance of Zintl Phases $(\text{Eu}_{0.5}\text{Yb}_{0.5})_{1-x}\text{Ca}_x\text{Mg}_2\text{Bi}_2$ by Band Engineering and Strain Fluctuation, *Proc. Natl. Acad. Sci. U. S. A.*, 2016, **113**(29), E4125–E4132.
 - 37 A. F. May, M. A. McGuire, J. Ma, O. Delaire, A. Huq and R. Custelcean, Properties of Single Crystalline AZn_2Sb_2 (A = Ca, Eu, Yb), *J. Appl. Phys.*, 2012, **111**(3), 33708.
 - 38 A. F. May, M. A. McGuire, D. J. Singh, J. Ma, O. Delaire, A. Huq, W. Cai and H. Wang, Thermoelectric Transport Properties of CaMg_2Bi_2 , EuMg_2Bi_2 , and YbMg_2Bi_2 , *Phys. Rev. B: Condens. Matter Mater. Phys.*, 2012, **85**(3), 035202.
 - 39 E. S. Toberer, A. F. May, B. C. Melot, E. Flage-Larsen and G. J. Snyder, Electronic Structure and Transport in

- Thermoelectric Compounds AZn_2Sb_2 ($A = Sr, Ca, Yb, Eu$), *Dalton Trans.*, 2010, **39**(4), 1046–1054.
- 40 H. Wang, Y. Pei, A. D. LaLonde and G. J. Snyder, Material Design Considerations Based on Thermoelectric Quality Factor, in *Thermoelectric Nanomaterials*, ed. K. Koumoto and T. Mori, Springer Berlin Heidelberg, 2013, pp. 3–32.
- 41 K. Imasato, S. D. Kang, S. Ohno and G. J. Snyder, Band Engineering in Mg_3Sb_2 by Alloying with Mg_3Bi_2 for Enhanced Thermoelectric Performance, *Mater. Horiz.*, 2017, **5**(1), 59–64.
- 42 W. G. Zeier, A. Zevalkink, Z. M. Gibbs, G. Hautier, M. G. Kanatzidis and G. J. Snyder, Thinking like a Chemist: Intuition in Thermoelectric Materials, *Angew. Chem., Int. Ed.*, 2016, **55**, 6826–6841.
- 43 H.-S. Kim, Z. M. Gibbs, Y. Tang, H. Wang and G. J. Snyder, Characterization of Lorenz Number with Seebeck Coefficient Measurement, *APL Mater.*, 2015, **3**(4), 41506.
- 44 U. Aydemir, A. Zevalkink, A. Ormeci, H. Wang, S. Ohno, S. Bux and G. J. Snyder, Thermoelectric Properties of the Zintl Phases $Yb_5M_2Sb_6$ ($M = Al, Ga, In$), *Dalton Trans.*, 2015, **44**, 6767–6774.
- 45 M. Thesberg, H. Kosina and N. Neophytou, On the Lorenz Number of Multiband Materials, *Phys. Rev. B*, 2017, **95**, 125206.